A Novel Fault Diagnosis Method for Multi-Stage Conversion Circuits Based on Data Fusion

Li Wang, *Member, IEEE*, Zidong Wang, *Fellow, IEEE*, Chao Xu, Guoping Lu and Liang Hua

Abstract—This paper addresses the research gap on fault diagnosis of multi-stage conversion circuits within analog circuit fault diagnosis. A diagnostic system is introduced, in which multi-point data fusion is combined with deep feature analysis, leading to the Integrated Dual-Axis Vision Transformer system. Initially, signals from multiple monitoring points are fused through the Integrated Wavelet Transform algorithm. Following this, deeper secondary data fusion is achieved by the Dual-Axis Vision Transformer algorithm, which utilizes a dual-axis observation encoder and an axial data decoder to interact between time-domain and frequency-domain features. This approach effectively analyzes signal characteristics, improving the accuracy of fault diagnosis. In experiments with the LLC Series Resonant Converter, both soft and hard faults were reliably diagnosed by the system, showing excellent accuracy, recall, and F1 score metrics.

Index Terms—Fault diagnosis, Multi-stage conversion circuit, Integrated wavelet transform, Dual-axis vision transformer, Data fusion.

I. INTRODUCTION

ELECTRICITY equipment in modern society continues to expand and diversify. Conventional single-stage conversion circuits no longer meet the varied requirements for high efficiency, stability, and low electromagnetic interference. By contrast, multi-stage conversion circuits have become the preferred option for electronic systems due to their superior ability to manage complex power conversion tasks, and this becomes evident in areas like computer power supplies, server power supplies, and electric vehicles, where they excel under frequent power fluctuations [7], [45]. However, these systems must operate continuously over long periods. The electronic components of multi-stage conversion circuits, as the system's power core, degrade over time due to prolonged electrothermal erosion. Once a soft fault transitions into a hard fault, it will lead to a complete system failure or even complete damage. Therefore, fault diagnosis for multi-stage conversion circuits is essential for guiding redundant power switching and ensuring system stability.

Previous circuit fault diagnosis methods include fault dictionary methods, parameter identification methods, fault verification methods, and approximation methods [40], [2], [32].

Li Wang, Chao Xu, Guoping Lu and Liang Hua are with the School of Electrical Engineering and Automation, Nantong University, Nantong 226019, China (e-mails: lwee@ntu.edu.cn; xcxiaoyao@stmail.ntu.edu.cn; lu.gp@ntu.edu.cn; hualiang@ntu.edu.cn).

Zidong Wang is with the Department of Computer Science, Brunel University London, UB8 3PH Uxbridge, U.K. (e-mail: Zidong.Wang@brunel.ac.uk)

However, these approaches typically rely on pre-constructed fault feature libraries or mathematical models for fault parameter estimation and verification. As a result, they often face certain limitations when applied to fault diagnosis in multi-stage converter circuits. These methods are generally challenged by insufficient diagnostic accuracy and limited applicability.

In recent years, numerous deep learning algorithms have emerged in data processing, leading many researchers to apply these intelligent methods to analog circuit fault diagnosis. Current diagnostic approaches typically involve three key components: fault signal collection, signal feature extraction, and the construction of classification models [30], [20], [8].

Fault signal collection involves setting feature points to gather target parameters such as voltage, current, and temperature, which provide foundational data for fault analysis. The pulse excitations have been inserted into the circuit in [3] so as to collect response signals from the output to represent circuit characteristics. In contrast, it has been argued in [25] that a single excitation signal is insufficient to convey the circuit state effectively, hence the use of multiple excitation responses has been proposed as circuit characteristics. However, these extraction methods are limited to specific feature points, and the selection of these points significantly affects the reliability of the data.

Signal feature extraction involves applying signal processing techniques to extract representative features from raw data that reflect the circuit's operational state [18]. In [21], the Wavelet Packet Transform (WPT) has been utilized to extract fault characteristic information from both the time and frequency domains. In [17], an improved Empirical Wavelet Transform (EWT) has been employed to capture the Amplitude Modulation-Frequency Modulation (AM-FM) components of the signal, effectively extracting various statistical features. To address the issue of small sample sizes, the Cross Wavelet Transform (XWT) has been used in [11] to capture features related to amplitude, phase, and coherence. These studies demonstrate that signal transformation theories excel in processing subtle signals.

Classification model construction involves building models using deep learning and optimization algorithms, where the extracted features are input into the model for training, creating an intelligent system for circuit fault diagnosis. Commonly used algorithms include early diagnostic algorithms, such as Support Vector Machines (SVM), Artificial Neural Network (ANN) and Autoencoders, as well as modern deep learning algorithms, such as Convolutional Neural Networks (CNN) and Long Short-Term Memory networks (LSTM) [33], [9],

TABLE I: COMPARISON OF CIRCUIT FAULT DIAGNOSIS STUDIES

Experimental circuit	Conversion stage	Failed component	Fault setting	Signal	Monitoring point	Feature extraction	Diagnostic model
Sallen-Key	None	Resistor/Capacitor	Simulation	Output voltage	1	WPT	SVMs [21]
Sallen-Key	None	Resistor	Simulation	Output voltage	1	EWT	ResNet [17]
Sallen-Key	None	Capacitor	Experiment	Output voltage	1	XWT	GANs [11]
Sallen-Key	None	Capacitor	Simulation	Output voltage	1	ELM	Autoencoder [33]
Sallen-Key	None	Resistor/Capacitor	Simulation	Output voltage	1	Math. statistic	CNNs [9]
Boost	Single-stage	Capacitor	Experiment	Output voltage	1	None	LSTM [13]
Boost	Single-stage	Capacitor	Simulation	Output voltage	1	None	SVMs [12]
Buck Boost	Single-stage	MOSFET	Simulation	Output voltage	1	SFMD	SVMs [10]
Three-Phase Inverter	Multi-stage	IGBT	Simulation	Output current	1	Math. statistic	ANN [16]
LLC	**Multi-stage**	**MOSFET**	**Experiment**	**Node voltage**	**3**	**IWT**	**DVIT**

- GANs, SVMs, CNNs: Represent the derived approaches of the corresponding basic methods.
- The bolded terms refer to the methods designed in this study.

[13]. These algorithms are capable of effectively identifying and classifying different types of signal features from data, enabling accurate fault diagnosis [23].

Based on the current state of research, as shown in Table I, the majority of studies have focused on fault diagnosis in filter circuits and single-stage converter circuits. However, there remains a significant gap in the field of fault diagnosis for multi-stage converter circuits. In multi-stage converter circuits, the fault features of front-end components are easily obscured by complex signals during the multi-stage signal transmission process, making previous methods and existing technologies ineffective for diagnosing such faults. Therefore, there is an urgent need for a novel diagnostic approach to address this issue.

This study is the first to approach fault diagnosis from the perspective of data fusion, employing a multi-point data acquisition strategy and proposing a fault diagnosis method for multi-stage converter circuits—Integrated Wavelet Transform with Dual-Axis Vision Transformer (IWT-DVIT). In this method, initial feature extraction and primary fusion of the electrical signal are performed using Integrated Wavelet Transform (IWT) in the signal feature section; in the model diagnosis section, the Dual-Axis Vision Transformer (DVIT) diagnostic model enables secondary fusion and accurate diagnosis of the input signal. The significant contributions of this paper are outlined as follows:

1) *IWT Method Design*: Building on the high-performance capabilities of Continuous Wavelet Transform (CWT) in fine signal analysis, this study proposes a data fusion scheme. The scheme achieves an initial dimensionality increase and feature extraction of the electrical signal by synchronously normalizing, time-frequency decomposing, and recombining multiple input signals.

2) *Innovative DVIT model*: To deeply fuse the time-frequency features provided by multiple electrical signals, this study designs a novel diagnostic model. The method includes a Dual-Axis Observation Encoder and an Axial Data Decoder. Through interactive time-domain and frequency-domain analysis, it achieves secondary fusion of deep data features and fault diagnosis.

3) *Physical Experiment Diagnosis*: This study selects an LLC series resonant converter as the target circuit for analysis and verification. Starting from the MOSFET fault mechanism, real fault states of the circuit are simulated at the physical level. Diagnostic performance
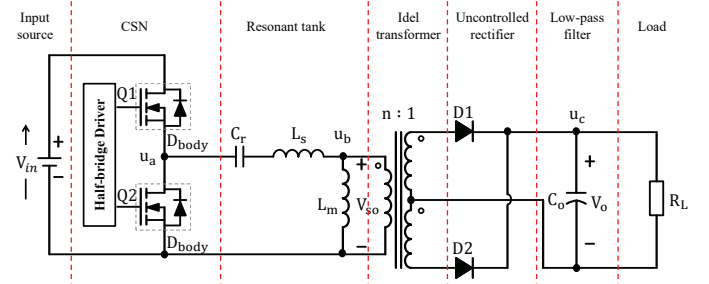

Fig. 1: LLC series resonant converter.

comparison experiments and variable load experiments are conducted to effectively validate the general applicability of the proposed approach.

The remainder of this paper is organized as follows: Section II examines the multi-stage conversion principles and fault mechanisms of the LLC Series Resonant Converter. Section III discusses the IWT-DVIT algorithm developed in this study in detail, focusing on data fusion and fault diagnosis. Section IV presents the experiments conducted on the target circuit, validating the method's accuracy. Finally, Section V concludes with a summary of the research findings.

II. CIRCUIT BACKGROUND

In this section, the operating principles and common causes of faults in the LLC Series Resonant Converter (a typical multi-stage conversion circuit) are analyzed.

A. Circuit Principle Analysis

The structural topology of the LLC Series Resonant Converter is shown in Fig. 1, which consists of seven components: the input source, a Controlled Switch Network (CSN), a resonant circuit, an ideal transformer, an uncontrolled rectifier, a low-pass filter, and a load [31]. This circuit represents a typical multi-stage conversion system, and its specific operating process is described as follows:

- *First Stage Conversion*: The input voltage source V_{in} is a DC voltage source. The switches Q1 and Q2 in the CSN are set with a 50% duty cycle, alternating to generate a square wave voltage u_a, completing the first stage of conversion.

- *Second Stage Conversion*: The resonant circuit, consisting of the resonant capacitor C_r, resonant inductor L_s, and leakage inductance L_m, processes the high-frequency
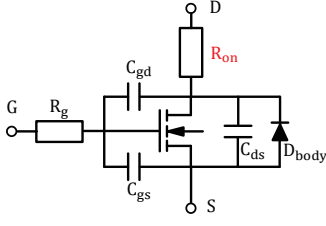
Fig. 2: MOSFET equivalent model.

square wave voltage. The voltage u_a passes through the resonant inductor L_s to generate a sinusoidal voltage u_b, completing the second stage of conversion.

- *Third Stage Conversion*: The ideal transformer performs a voltage transformation on the sinusoidal voltage u_b, and the output is rectified into a DC voltage using an uncontrolled rectifier. The DC voltage is then filtered through a low-pass filter with a capacitor C_o to remove high-frequency ripple, resulting in the DC output voltage u_c, completing the third stage of conversion.

In summary, the LLC Series Resonant Converter is a typical multi-stage conversion circuit. Additionally, multi-stage conversion circuits include the Flyback Converter, Phase-Shifted Full Bridge (PSFB) Converter, Dual Active Bridge (DAB) Converter, and other circuits formed by continuous combinations of basic converters. For ease of analysis, the following content focuses on the LLC Series Resonant Converter as a representative multi-stage conversion circuit for this study.

B. Circuit Fault Analysis

Compared to other passive components, a significant number of faults in LLC Series Resonant Converter are concentrated in the power MOSFETs. Their equivalent model is shown in Fig. 2, which includes the gate resistance R_g, conduction resistance R_{on}, gate-drain capacitance C_{gd}, gate-source capacitance C_{gs} and drain-source capacitance C_{ds}.

When the circuit operates continuously at high frequencies, the frame, chip, and die attach of the MOSFET experience cyclical thermal stress, causing a gradual increase in conduction resistance, which results in soft failures. In [15], the functional relationship between conduction resistance and temperature has been provided as follows:

$$R_{on}(T_j) = (V_{gs} - V_{th}) \frac{R_{on}(T_0)}{v_{gs} - V_{th}} \left(\frac{T_j}{T_0}\right)^r \quad (1)$$

where T_j is the MOSFET junction temperature, V_{gs} is the nominal conduction voltage, V_{th} is the threshold voltage and r is a constant (typically 2.65). As the operating time increases, the plastic deformation caused by thermal stress accumulates, eventually leading to the following frequently occurred hard failure (Q1 as an example):

- *Gate-drain short circuit*: The input voltage is directly applied to the gate of Q1, raising the minimum value of the square wave voltage u_a, decreasing the rate of change in current through L_p, reducing the amplitude of the sinusoidal voltage u_b, and diminishing the DC output voltage u_c.
- *Gate-source short circuit*: The drive signal is directly applied to the source of Q1. The square wave voltage u_a
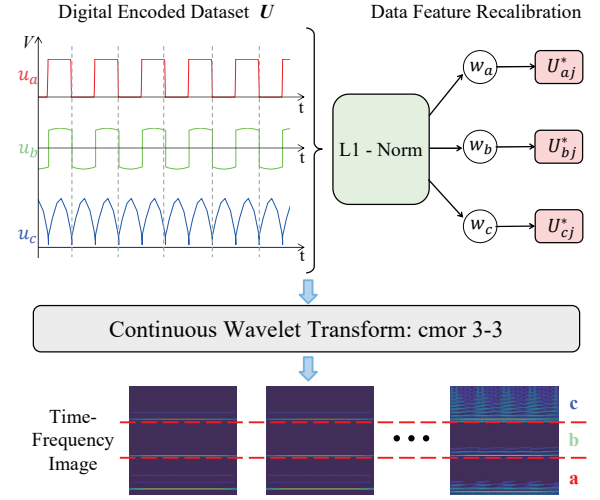

Fig. 3: IWT method based on L_1-norm.

continues to output a periodic DC waveform, but with reduced amplitude and increased harmonics. This also results in a reduced amplitude of the sinusoidal voltage u_b and increased harmonics, leading to a minimal DC output voltage u_c.

- *Drain-source open circuit*: There is no voltage between the drain and source of Q1, the u_a node receives only a minimal current from the drive signal, resulting in extremely low voltage amplitude. This also leads to a very small amplitude of the sinusoidal voltage u_b, increased harmonics, and a minimal DC output voltage u_c.
- *Drain-source short circuit*: Q1 behaves as if it is continuously on. When Q2 conducts, the input source triggers a short circuit protection, and the circuit ceases operation.

III. DIAGNOSTIC SYSTEM

Building on the analysis from the previous section, this section introduces the IWT-DVIT diagnostic system, which utilizes multi-point data fusion for fault analysis. This method comprises three stages: primary data fusion, secondary data fusion, and data diagnosis.

A. Primary Data Fusion

In the early stages of data fusion, fault features are often concealed within the raw signals from the three monitoring points. Therefore, the fusion process should avoid losing any potential fault characteristics. Considering that the L1 norm is less sensitive to outliers in anomaly detection and is effective in extracting high-frequency features from sparse data, this study proposes an IWT method based on the L_1-norm for feature re-calibration, enabling effective data fusion. The specific process is illustrated in Fig. 3.

First, voltage waveforms of u_a, u_b, and u_c under normal conditions and various fault types are collected and recorded as the digital encoded dataset U:

$$\boldsymbol{U} = \begin{bmatrix} U_{a1} & U_{b1} & U_{c1} & 1 \\ U_{a2} & U_{b2} & U_{c2} & 2 \\ U_{a3} & U_{b3} & U_{c3} & 3 \\ U_{a4} & U_{b4} & U_{c4} & 4 \\ U_{a5} & U_{b5} & U_{c5} & 5 \end{bmatrix} \quad (2)$$

In the formula, U_{ij} (where $i = a, b, c$ and $j = 0, 1, 2, ...9$) represents the time-aligned voltage data collected from the circuit under the j type of condition. Subsequently, the data U_{ij} are normalized:

$$U_{ij}^{\text{norm}} = \frac{U_{ij} - \mu}{\sigma} \tag{3}$$

Here, μ and σ represent the mean and standard deviation of the signal, respectively. As shown in Fig. 3, based on the L_1-norm, the distribution weights for the three signals can be calculated as follows:

$$w_a = \frac{\exp\left(\left\|U_{aj}^{\text{norm}}\right\|_1\right)}{\exp\left(\left\|U_{aj}^{\text{norm}}\right\|_1\right) + \exp\left(\left\|U_{bj}^{\text{norm}}\right\|_1\right) + \exp\left(\left\|U_{cj}^{\text{norm}}\right\|_1\right)} \tag{4}$$

Similarly, the distribution weights w_b and w_c are calculated, and the original signals are recalibrated to obtain the processed data U_{ij}^*:

$$\begin{aligned} U_{aj}^* &= U_{aj}^{\text{norm}} \cdot w_a \\ U_{bj}^* &= U_{bj}^{\text{norm}} \cdot w_b \\ U_{cj}^* &= U_{cj}^{\text{norm}} \cdot w_c \end{aligned} \tag{5}$$

Finally, CWT is applied synchronously to the three datasets to obtain and integrate time-frequency images [5]:

$$IWT = \frac{1}{\sqrt{|s|}} \int_{-\infty}^{\infty} U^*(t) \cdot \psi\left(\frac{t - \tau}{s}\right) dt \tag{6}$$

where U^* represents the digitally encoded data set composed of U_{ij}^*, ψ denotes the wavelet basis function, s is the scale parameter and τ is the translation parameter.

In selecting the wavelet basis function, considering the specific characteristics of the three different types of signals, the IWT algorithm requires a wavelet basis function that can simultaneously apply to all these signals. This study compares commonly used wavelet basis functions in fault diagnosis:

- *Daubechies Wavelet (db)*: While it has good localization properties in the time domain, its frequency domain resolution is poor, making it challenging to effectively handle multi-frequency components [27].
- *Symlet Wavelet (sym)*: Symmetric in nature, it is suitable for stationary signals but lacks flexibility when handling non-stationary signals, leading to the loss of high-frequency information [24].
- *Complex Morlet Wavelet (cmor)*: It has strong adaptability and can handle signals with different characteristics. It provides a unified time-frequency analysis framework, capturing both amplitude variations and phase changes, including phase misalignment [41].

Based on the above analysis, this study chooses the cmor as the wavelet basis function for IWT. Additionally, the cmor can adjust the center frequency and bandwidth parameters according to the monitoring points to meet the requirements for initial data fusion. Therefore, using the IWT method, this study successfully fuses the three signals into a unified time-frequency representation, providing a comprehensive view for synchronously analyzing the fault features of all signals.

B. Secondary Data Fusion

After the input signals undergo initial data fusion, surface-level features are combined. However, this fusion only reveals the surface characteristics of the signals and cannot effectively capture the relationships of deeper features within the signals. Fault characteristics remain embedded in the time-frequency images of the electrical signals, manifesting as distinct amplitude fluctuations in the time domain and synchronized multiple harmonics in the frequency domain. To further enhance the degree of signal fusion and extract deeper fault features from both the time and frequency domains, this study proposes a DVIT method. This method consists of two main modules: the Dual-Axis Observation Encoder and the Axial Data Decoder.

Dual-Axis Observation Encoder: The dual-axis observation encoder extracts features by encoding data bidirectionally from both vertical and horizontal axes. Specifically, the process starts with axial convolutions applied to the input feature map $X \in \mathbb{R}^{B \times C \times H \times W}$:

$$\begin{aligned} V_{\text{out}}^i &= \text{ReLU}\left(BN\left(W_v^i * X + b_v^i\right)\right) \\ H_{\text{out}}^i &= \text{ReLU}\left(BN\left(W_h^i * X + b_h^i\right)\right) \end{aligned} \tag{7}$$

where W_v and W_h represent the weights of the vertical and horizontal kernels at the i scale, respectively, while b_v and b_h denote the biases for the vertical and horizontal kernels, respectively. The symbol $*$ denotes the convolution operation. The scales of the convolution kernels are $(nH \times 1)$ and $(1 \times nW)$ strip convolutions, where n represents the number of layers, with values of $\frac{1}{3}$, $\frac{2}{3}$ and $\frac{3}{3}$, determined by the number of fusion data points.

Next, the encoded data at the three scales are fused separately along the vertical and horizontal axes:

$$\begin{aligned} V_{\text{merged}} &= \text{Concat}\left(V_{\text{out}}^1, V_{\text{out}}^2, V_{\text{out}}^3\right) \\ H_{\text{merged}} &= \text{Concat}\left(H_{\text{out}}^1, H_{\text{out}}^2, H_{\text{out}}^3\right) \end{aligned} \tag{8}$$

where Concat represents the concatenation operation along the channel dimension, combining feature maps from different scales to create the fused axial feature matrix. This matrix comprehensively reflects the fault features extracted under dual-view multi-scale conditions, capturing both synchronized encoded observations in the time and frequency domains, and providing comprehensive information for subsequent fault analysis.

Axial Data Decoder: When a fault occurs in the converter, highly correlated synchronous disturbances are generated in both the time and frequency domains of the electrical signals. Analyzing only one perspective (time domain or frequency domain) is insufficient to fully extract the fault features. It is only through the interactive analysis of both perspectives that deep fault characteristics can be thoroughly mined and extracted [38]. The axial data decoder solves the axial feature matrix by deeply integrating information from both the time and frequency domains. It consists of two modules: the Axis-Cross Attention module and the H-W Attention module.

Axis-Cross Attention module: This module, as illustrated in Fig. 4(a), performs attention operations on the vertical X and horizontal Y information, generating a fused feature matrix Z after aggregating these two types of data flows. This module
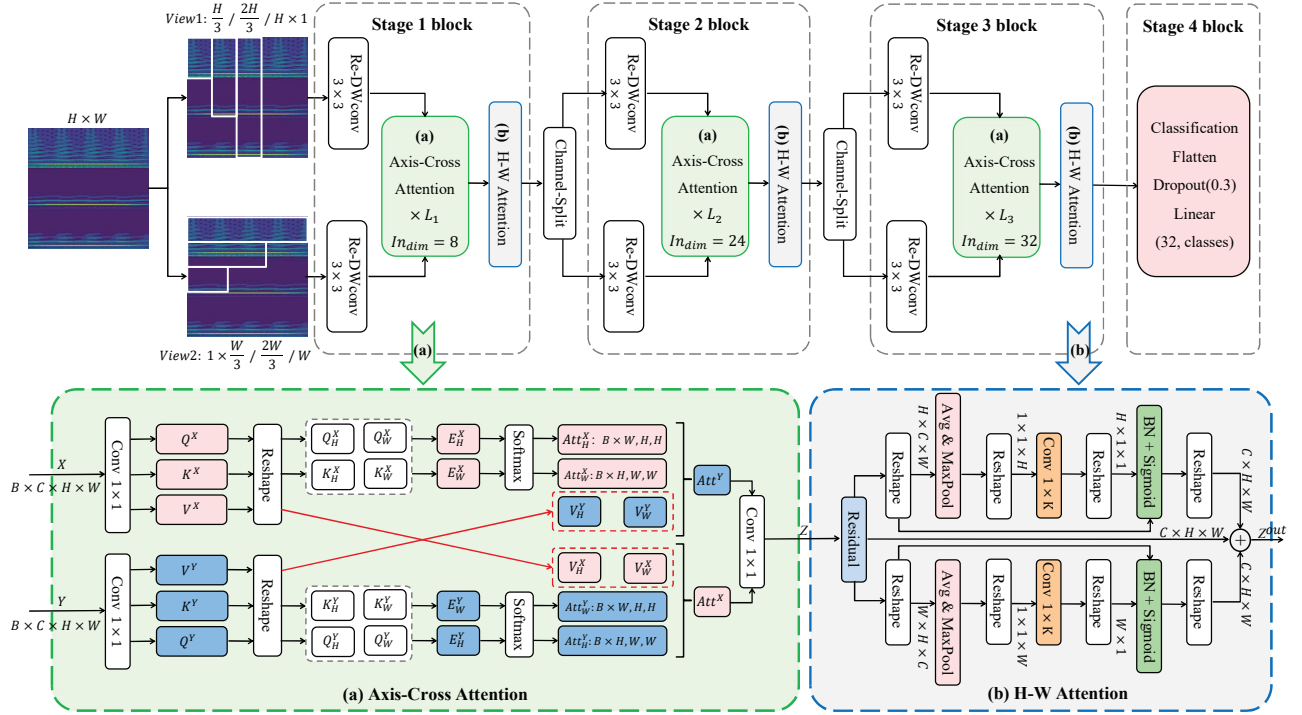
Fig. 4: Schematic illustration of the DVIT model.

Algorithm 1 Axial Cross Attention Mechanism

1: **Input:** Feature tensors $X, Y \in \mathbb{R}^{B \times C \times H \times W}$
2: **Setting:** Learnable parameters γ_x, γ_y
3: **Define:** Dimension $D = C/8$
4: **Step 1:** Generate Q, K and V
5: $\quad Q_X, K_X, V_X = \mathrm{Conv}_{1x1}(X)$
6: $\quad Q_Y, K_Y, V_Y = \mathrm{Conv}_{1x1}(Y)$
7: **Step 2:** Reshape Q, K and V
8: $\quad$ Feature tensors X:
9: $\quad Q_{hx}, Q_{wx} = \mathrm{Reshape}(Q_X, [B \times W, D, H])$
10: $\quad K_{hx}, K_{wx} = \mathrm{Reshape}(K_X, [B \times W, D, H])$
11: $\quad V_{hx}, V_{wx} = \mathrm{Reshape}(V_X, [B \times W, C, H])$
12: $\quad$ Feature tensors Y:
13: $\quad Q_{hy}, Q_{wy} = \mathrm{Reshape}(Q_Y, [B \times H, D, W])$
14: $\quad K_{hy}, K_{wy} = \mathrm{Reshape}(K_Y, [B \times H, D, W])$
15: $\quad V_{hy}, V_{hy} = \mathrm{Reshape}(V_Y, [B \times H, C, W])$
16: **Step 3:** Calculate Activation Energy Scores
17: $\quad E_{hx} = Q_{hx} \times K_{hx}^T/\sqrt{D}$, $E_{wx} = Q_{wx} \times K_{wx}^T/\sqrt{D}$
18: **Step 4:** Compute Attention Weights
19: $\quad Att_{hx} = \mathrm{Softmax}(E_{hx}),\ Att_{wx} = \mathrm{Softmax}(E_{wx})$
20: **Step 5:** Compute Attention Output
21: $\quad Attx = Att_{hx} \times V_{hx} + Att_{wx} \times V_{wx}$
22: **Step 6:** Perform similar operations on Y to obtain $Atty$
23: **Step 7:** Compute Final Output
24: $\quad Z = \mathrm{Conv}_{1x1}(\gamma_x \times Attx + \gamma_y \times Atty)$
25: **Output:** Feature tensors $Z \in \mathbb{R}^{B \times C \times H \times W}$

---

interacts with the two input matrices, each utilising the other's Query(Q) and Key(K) to adjust its own Value(V), with the detailed process described in Algorithm. 1.

H-W Attention module: For the aggregated feature matrix Z, this study has developed a convolutional attention module. As shown in Fig. 4(b), this module independently learns the high-frequency features in the vertical and horizontal directions, further enhancing the network's local perceptual abilities in these two dimensions.

First, the input matrix Z undergoes both average pooling and global pooling. The results of these pooling operations are then weighted and fused together:

$$Z_p = w_0 \cdot \mathrm{AvgPool}(Z) + w_1 \cdot \mathrm{MaxPool}(Z) \quad (9)$$

where w_0 and w_1 are learnable weights. Following this, a gated processing unit is defined, which uses one-dimensional convolution to encode data along the vertical and horizontal directions separately, generating attention maps:

$$A^H(Z), A^W(Z) = \mathrm{Sigmoid}\left(\mathrm{Conv}1D_1^k\left(Z_p\right)\right) \quad (10)$$

The convolution is a $1 \times k$ strip convolution with the stride fixed at 1. This setup allows for the recalibration of the original input Z:

$$\begin{aligned} Z^H &= A^H(Z) \odot Z \\ Z^W &= A^W(Z) \odot Z \end{aligned} \quad (11)$$

where $\odot$ denotes element-wise multiplication. Finally, this paper introduces a residual connection and conduct an average fusion of the feature matrices from both directions to obtain the adjusted feature output:

$$Z^{\mathrm{out}} = \frac{1}{3}\left(Z^H + Z^W + Z\right) \quad (12)$$

C. Data Diagnosis

Synthesizing the aforementioned modules, this study has developed a data diagnostic architecture, illustrated in Fig. 4.

TABLE II: CIRCUIT COMPONENT PARAMETERS

Component	Model number / Parameter value
V_{in}	12v
C_r	2μF
L_s	4.7μH
L_m	16μH
C_o	470μF
Q1/Q2	IRF540N
D1/D2	SS54C
Turns radio	1.2 : 1 : 1

- **Operating frequency**: $f_s = 52$ kHz.
- **Duty cycle**: $D = 50\%$.

This architecture is based on the generic Vision Transformer (VIT) visual architecture and is divided into four primary stages. The first three stages involve continuous scale upsampling of data to accomplish information fusion and feature extraction. In the final stage, data features are mapped to classification results using an adaptive fully connected classification head.

The structure of the classification head includes:

- Adaptive Pooling Layer: This layer pools the feature maps to produce a fixed-size feature vector.
- Flatten Layer: This layer flattens the pooled feature vector into a one-dimensional vector.
- Dropout Layer: This layer is used to reduce the risk of overfitting.
- ReLU Fully Connected Layer: This layer applies a non-linear transformation to the flattened feature vector and outputs the classification results.

Through the processing of the above four stages, the data diagnostic architecture is able to effectively extract and integrate deep features, allowing for accurate classification of various types of faults.

IV. EXPERIMENTAL VERIFICATION

This section presents the experimental setup of this study and provides a detailed analysis of the experimental results.

A. Experimental Environment

The hardware platform for the experiment is shown in Fig. 5, with the parameters of the LLC target circuit components provided in Table II. The data acquisition setup includes a peripheral acquisition circuit designed to extract voltage signals using the operational amplifier chip RS8754 and the RMS detection chip AD637. The ADC module is implemented with the NI USB-6001 data acquisition card, offering a sampling rate of 1 MHz, and synchronized data acquisition is managed by an upper computer system.

The testing algorithms for this experiment are implemented in Pytorch-2.1 and executed on an Ubuntu-based experimental platform. The hardware configuration includes an Intel Core i9-13900K CPU and an NVIDIA GeForce RTX 3090 GPU.

B. Fault Setting

In contrast to software simulation experiments, as shown in Fig. 6, this study simulates hardware faults on a physical model by adding new devices in series or parallel. For the simulation of soft faults, fault points are set where the conduction
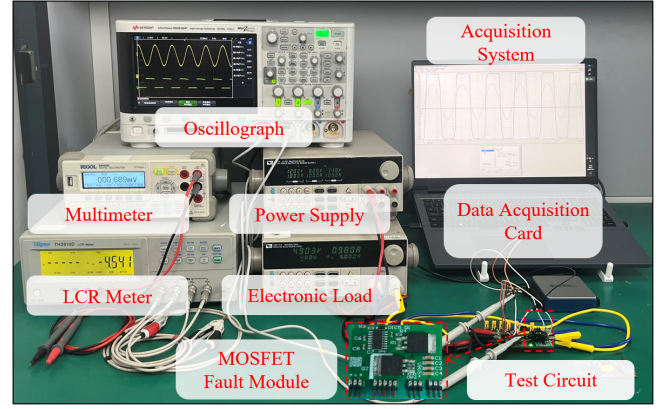

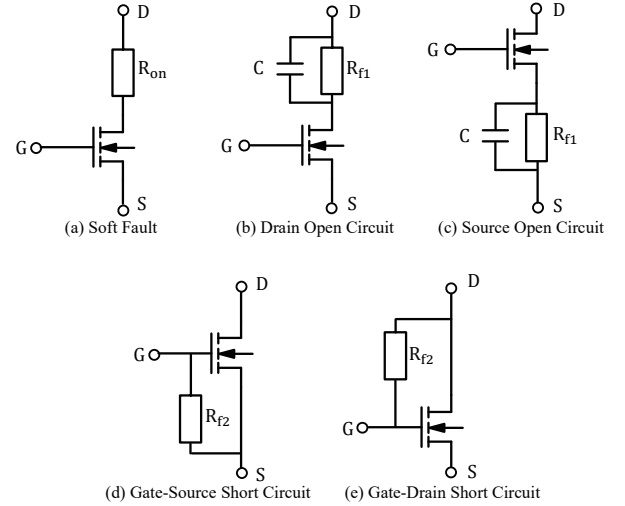Fig. 5: Hardware experimental platform.

Fig. 6: Fault simulation programmes. For soft faults in Figure (a), the conduction resistance R_{on} of the IRF540N is set to 130% and 160% of its nominal 44 mΩ. For open-circuit faults in Figures (b) and (c), an ultra-small capacitor C_f is used at 2e-10 μF, with an ultra-large resistor R_{f1} at 10 MΩ. For short-circuit faults in Figures (d) and (e), an ultra-small resistor R_{f2} is set to 1e-6 Ω.

resistance is 30% and 60% higher than the nominal values, with a resistance tolerance of $\pm2\%$. In the simulation of hard faults, the most frequent power MOSFET faults (such as drain-source open circuit, gate-source short circuit, and gate-drain short circuit) are selected as fault points.

The final identified fault categories are shown in Table III. For each category, 800,000 data points are collected from the three monitoring points to form the total experimental sample set. This data set is then split into a training set and a test set at a ratio of 4:1.

C. Primary Data Fusion Effect

To achieve efficient optimization of the two key parameters (bandwidth parameter and center frequency) of the cmor wavelet basis function in the IWT algorithm, this study proposes a distinctiveness D as an evaluation metric, based on the theory of Gray Level Co-occurrence Matrix (GLCM) [28]. The process is as follows:

Initially, for each time-frequency image P, we compute the statistical measures from its GLCM, including contrast (CO),

TABLE III: CONVERTERS FAILURE RATINGS DATA

Fault category	Classes	Q1	Q2
Soft fault	a0	44mΩ	44mΩ
	a1	58.08–56.32mΩ	44mΩ
	a2	71.28–69.52mΩ	44mΩ
	a3	44mΩ	58.08–56.32mΩ
	a4	44mΩ	71.28–69.52mΩ
	a5	58.08–56.32mΩ	58.08–56.32mΩ
	a6	58.08–56.32mΩ	71.28–69.52mΩ
	a7	71.28–69.52mΩ	58.08–56.32mΩ
	a8	71.28–69.52mΩ	71.28–69.52mΩ
Hard fault	b0	Normal	Normal
	b1	DO	Normal
	b2	SO	Normal
	b3	GS	Normal
	b4	GD	Normal
	b5	Normal	DO
	b6	Normal	SO
	b7	Normal	GS
	b8	Normal	GD

- **DO**: Drain Open Circuit. **SO**: Source Open Circuit.
- **GS**: Gate-Source Short Circuit. **GD**: Gate-Drain Short Circuit.

TABLE IV: IWT PARAMETER OPTIMISATION

Distinctiveness (D)	Bandwidth Parameter				
	0	1	2	**3**	4
Center Frequency	1	0.9112	1.1035	1.3596	1.2879
	2	0.9275	1.2209	1.4052	1.2934
	3	0.9693	1.3557	**1.5162**	1.3843
	4	0.9518	1.2324	1.4951	1.3650

- **Centre Frequency**: in the Wavelet Tool Library, the unitless normalised frequency.

dissimilarity (DI), homogeneity (HO), and energy (EN), to form a feature vector **F**.

$$\mathbf{F} = [CO(P), DI(P), HO(P), EN(P)] \tag{13}$$

Next, calculate the intra-class and inter-class distances respectively:

$$\text{Intra} = \frac{1}{N(N-1)} \sum_{i=1}^{N} \sum_{j=i+1}^{N} \|\mathbf{F}_i - \mathbf{F}_j\| \tag{14}$$

$$\text{Inter} = \frac{2}{C(C-1)} \sum_{a=1}^{C} \sum_{b=a+1}^{C} \frac{1}{N^2} \sum_{i=1}^{N} \sum_{j=1}^{N} \left\|\mathbf{F}_a^i - \mathbf{F}_b^j\right\| \tag{15}$$

In the formula, N represents the number of samples within a class, C denotes the total number of classes, and the term represents the Euclidean distance between feature vectors. From this, the distinctiveness D can be calculated.

$$D = \frac{\text{Inter}}{\frac{1}{C} \sum \text{Intra}} \tag{16}$$

A larger value of D indicates a better transformation effect, meaning the time-frequency images are more effective for model classification and diagnosis. The parameter optimization results are shown in Table IV. The data indicates that for LLC converter faults in this study, the optimal parameter selection is (3-3), with a maximum distinction degree of 1.5162.

Remark 1: Fig. 7 (a) presents the time-frequency transformation images for typical soft faults ($a0$, $a5$) under fault conditions, and Fig. 7 (b) shows the voltage time-sequence
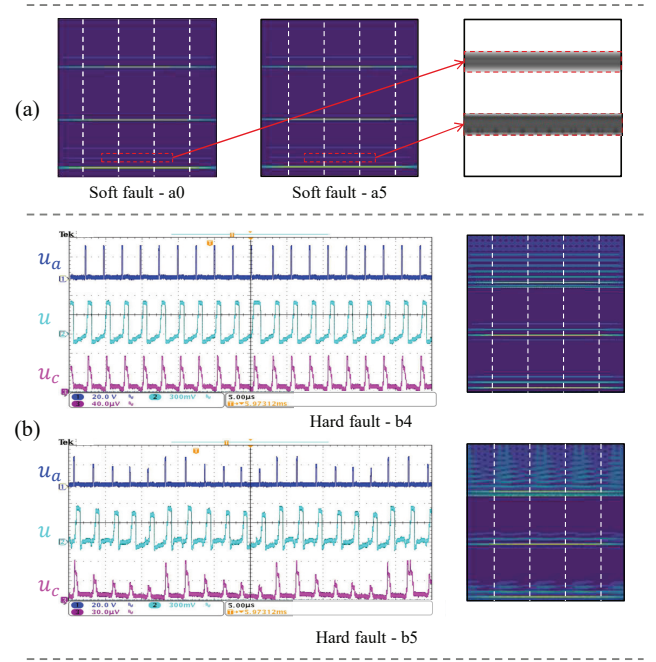

Fig. 7: Converters fault time-frequency image.

waveforms and time-frequency transformation images for typical hard faults ($b4$, $b5$). Each mixed time-frequency image is divided into three sections, displaying the data transformation results for monitoring points a, b, and c, respectively.

By comparing the time-frequency images for soft faults $a0$ and $a5$, when the conduction resistance of Q1 increases by 30%, the data at points b and c show no significant changes. However, a periodic jitter appears in the second frequency band of the data at point a. By comparing the voltage waveform images for hard faults $b4$ and $b5$, when the LLC circuit system is subjected to gate-source short-circuit and drain open-circuit faults, the voltage time-sequence waveforms at monitoring points a, b, and c all exhibit significant jumps. Signal observations show that these waveforms exhibit periodic irregular jumps, and the time-frequency transformation images reveal that the output signal contains substantial periodic high-frequency noise.

In summary, the time-frequency images produced by primary data fusion effectively integrate the characteristics of the three monitoring points, revealing features that might be overlooked in single time-series signals. The concept of multi-point data fusion is critical for fault identification in analog circuits.

D. Diagnostic Performance Analysis

To effectively analyze the role of data fusion and model algorithms in the fault diagnosis of multi-stage converter circuits, this section designs experiments on data fusion, model comparison, and varying load conditions for comprehensive validation.

Data Fusion Experiment: This study establishes five data scenarios based on the degree of input data fusion and selects each type from the test set for 10 random trials with 100,000
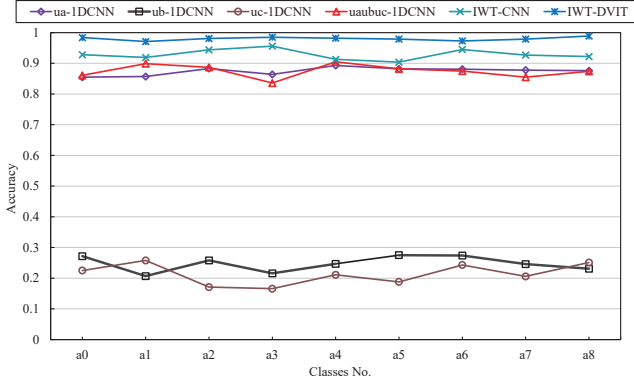
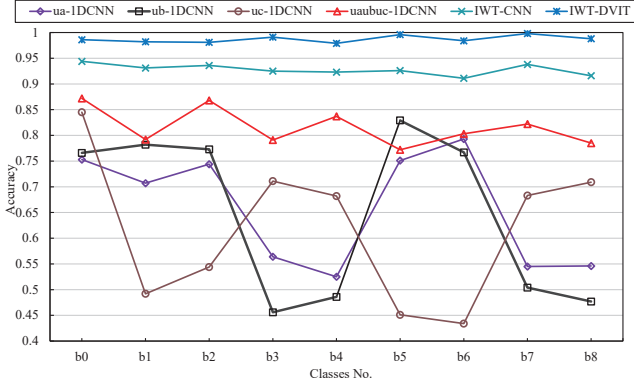Fig. 8: Comparison of soft fault experimental results.

Fig. 9: Comparison of hard fault experimental results.

points each. The results of these experiments are presented in Fig. 8 and Fig. 9.

The data scenarios include:

- ua-1DCNN: 1D Convolutional Neural Network (1DCNN) [34] with signal a input alone.
- ub-1DCNN: 1DCNN with signal b input alone.
- uc-1DCNN: 1DCNN with signal c input alone.
- uaubuc-1DCNN: Three-channel 1DCNN with simultaneous input of signals a, b, and c.
- IWT-CNN: CNN incorporating IWT preprocessing.
- IWT-DVIT: The algorithm model of this study.

Fig. 8 presents the results of the soft fault experiments. Among the three single-input 1DCNN models, the model using only the a signal shows significantly higher accuracy than those using signals b and c. This aligns with the principles of the LLC converter, where the a point signal, not being transformed by the resonant capacitor, retains more comprehensive feature information. However, when the signals from monitoring points a, b, and c are simultaneously input into the three-channel 1DCNN model, the accuracy does not improve, which is mainly because the b and c signals do not provide useful classification information and instead reduce the efficiency of the model's parameter tuning.

Remark 2: After introducing the IWT preprocessing, the CNN model achieved an average test accuracy of 92.8%. Compared to time-series signals, time-frequency images further uncovered the potential fault features. The IWT algorithm enhanced the data features of the time-frequency images, effectively improving the model's recognition accuracy for soft faults.

TABLE V: HYPERPARAMETER PERFORMANCE

Block	Dropout	Acc	Loss	PS(MB)
2	0.2	0.8454	0.1675	6.97
2	0.3	0.8753	0.1330	6.97
2	0.4	0.8136	0.2077	6.97
3	0.2	0.9813	0.0099	17.34
3	**0.3**	**0.9901**	**0.0063**	**17.34**
3	0.4	0.9652	0.0293	17.34
4	0.2	0.9237	0.0795	27.82
4	0.3	0.9544	0.0359	27.82
4	0.4	0.9138	0.0905	27.82

- PS: Parameter Size, used to measure the complexity of a model.
- The optimal hyperparameter settings are highlighted in bold to emphasize the results of the optimization.

Fig. 9 presents the results of the hard fault experiments. Comparing the three single-input 1DCNN models, the models using signals a and b are more effective at identifying open-circuit faults, while the model using signal c performs better at detecting short-circuit faults. This is because, in the LLC converter, open-circuit faults involving Q1 and Q2 tend to cause mode confusion at point c, whereas short-circuit faults lead to mode confusion at points a and b. When integrating data from all three signals, the average accuracy of the three-channel 1DCNN increases to 81.5%.

Remark 3: Consistent with the soft fault experimental results, the IWT-CNN model with IWT preprocessing achieved an average accuracy of 92.7%, further demonstrating that the time-frequency images derived from the IWT algorithm have a significant advantage in diagnostic performance and accuracy compared to directly inputting time-series signals.

Furthermore, the IWT-DVIT algorithm proposed in this study is introduced. Experimental results show that when the fault point is close to the monitoring point, the diagnostic accuracy of the IWT-DVIT algorithm does not significantly improve compared to single-point data diagnosis algorithms. However, when the theoretical distance between the fault point and the monitoring point is relatively large, the advantages of the IWT-DVIT algorithm become more apparent. Therefore, the algorithm developed in this study is particularly suitable for fault diagnosis of multi-stage converter circuits, while it may have certain limitations for circuits with simpler signal conversion, such as Buck and Boost circuits.

Model Comparison Experiment: Before the formal comparison experiments, this study determined the optimal hyperparameters for the model's number of blocks and dropout value through preliminary experiments. The pre-experiments used soft fault data and hard fault fusion datasets, each containing 500 time-frequency images per class. The experimental results are shown in Table V.

The pre-experiment results indicate that, when testing the time-frequency image features of soft and hard faults in the circuit, the model achieves the highest diagnostic accuracy and the smallest average test loss when the number of fusion blocks is set to 3. Furthermore, as the number of blocks increases, the number of channels adds up, leading to a significant increase in the model's PS. Therefore, from the perspective of model efficiency, the number of blocks should not be too large. The dropout layer is closely related to the model's generalization ability. Although the average loss differences are not significant, when the dropout rate is set

TABLE VI: MODEL COMPARISON EXPERIMENTAL RESULTS

Model	Performance indicators			Efficiency indicators	
	ACC	R	F1	PS(MB)	IT(s/100)
1DCNN [34]	0.8643	0.86	0.87	4.55	1.031
SVM [12]	0.7753	0.76	0.78	2.71	1.322
LSTM [13]	0.8226	0.82	0.82	6.21	4.465
CNN [9]	0.9288	0.92	0.93	14.55	7.908
EffNetV2 [26]	0.9462	0.95	0.94	23.12	8.224
VIT [39]	0.9022	0.83	0.83	25.10	8.813
SwinT [14]	0.9554	0.94	0.95	16.13	8.238
KTPP [43]	0.9697	0.96	0.95	29.9	10.683
G-Mamba [29]	0.9708	0.98	0.97	23.17	8.530
CAS-ViT [44]	0.9815	0.97	0.95	25.63	8.727
DVIT	**0.9901**	**0.98**	**0.99**	**17.34**	**9.337**

- **One-dimensional data processing model**: 1DCNN, SVM, LSTM.
- **Two-dimensional data processing model**: CNN, EfficientNetV2 (EffNetV2), Vision Transformer (VIT), Swin Transformer (SwinT), KAN Transformer with Pyramid Prompts (KTPP), GroupMamba (G-Mamba), Convolutional Additive Self-attention Vision Transformers (CAS-ViT).
- **IT**: Inference Time, used to gauge the model's real-time performance and efficiency.
- The experimental results of the algorithm proposed in this study are shown in bold to highlight its performance advantages.

TABLE VII: VARIABLE LOAD DIAGNOSTIC TASKS

Datasets	Loads	STSE		DTSE	
		Train	Test	Train	Test
A	5Ω	A	BC	AB	C
B	10Ω	B	AC	AC	B
C	15Ω	C	AB	BC	A

- **STSE**: Single-training-set experiment.
- **DTSE**: Dual-training-set experiment.

Fig. 10: Variable load experiment.

to 0.3, the model achieves the highest average diagnostic accuracy, and its generalization ability on the fault dataset is also superior.

In the formal experiments, this study selected existing circuit fault diagnosis models for comparison, covering both one-dimensional and two-dimensional data diagnosis algorithms. The experimental design includes ablation experiments and comparative experiments, as shown in Table VI. By measuring the accuracy, recall, and F1 score of each model, this study evaluates the performance of the various diagnostic models. The specific calculation formulas are as follows:

$$Acc = \frac{TP + TN}{TP + TN + FN + FP}$$
$$R = \frac{TP}{TP + FN} \quad (17)$$
$$F1 = \frac{2TP}{2TP + FP + FN}$$

where TP represents true positives, TN represents true negatives, FP represents false positives, and FN represents false negatives. In addition, the experiment also records the model's PS and IT as efficiency indicators to further assess the practicality of the diagnostic models.

The traditional one-dimensional data diagnosis algorithms perform poorly overall due to their inability to effectively fuse feature information from multiple monitoring points. Specifically, 1DCNN, with its strong feature extraction capability, achieved an average accuracy of 86%, outperforming SVM and LSTM.

In the new two-dimensional data diagnosis algorithms, the average accuracy of the diagnostic model was significantly improved by introducing IWT for image fusion. Compared to CNN, EffNetV2 demonstrated certain advantages in structural design, with the average accuracy increasing by 2%.

Although the VIT model effectively enhanced feature processing capability through its self-attention mechanism, its performance did not meet expectations due to the large computational load, with a final accuracy of 90.2%. In contrast, the
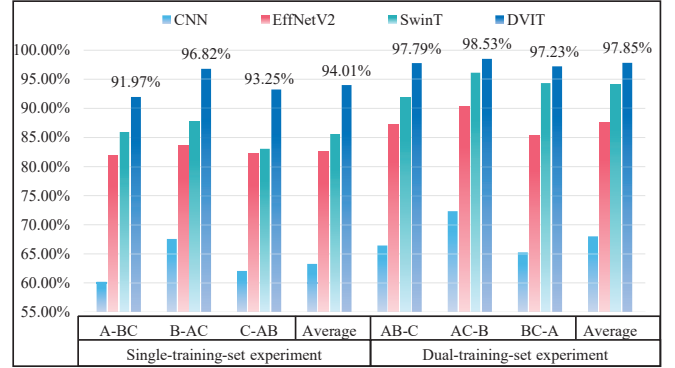
SwinT, based on an improved architecture, achieved a higher accuracy of 94.6%, demonstrating a significant performance improvement.

Remark 4:The latest high-performance model based on the VIT architecture, CAS-ViT, also shows excellent performance, achieving 98.15% accuracy after preliminary pre-training. In addition, the latest research under other architectures, such as KTPP and G-Mamba, has made breakthroughs in overall accuracy with the support of the latest schemes. However, these models experienced fluctuations in category accuracy and overfitting issues during the later stages of training, ultimately reaching accuracies of only 96.97% and 97.08%. In contrast, the DVIT model designed in this study, combined with multi-point data fusion techniques, successfully achieved a high diagnostic accuracy of 99.01%.

Moreover, the efficiency metrics indicate that two-dimensional data processing models are generally more complex than one-dimensional models, with the PS of the DVIT model being slightly higher than other CNN-based two-dimensional models. In terms of execution speed, although the IT of the DVIT model is on average 1 s slower than other two-dimensional models, the time difference per image is only 0.01 s, which has almost no impact on real-time diagnostic tasks. The experimental results show that the DVIT model significantly outperforms existing methods in the overall diagnostic performance of multi-stage converter circuits, demonstrating higher accuracy.

Variable Load Experiment: This experiment conducted a generalization test of the proposed method under varying load conditions. By simulating a ±50% change in the converter's standard output load, fluctuations in the converter's operating state were simulated. As shown in Table VII, the experiment set up fault diagnosis tasks with biased samples and comprehensively compared the diagnostic performance of four algorithms: CNN, EffNetV2, SwinT, and DVIT. The experimental results are shown in Fig. 10.

In the single dataset experiment, the traditional CNN method exhibited a low average accuracy of only 63.28%, due to the large difference in local features between the training samples and test samples. This issue became more pronounced when the dataset and test set had a wide load variation. However, when the models were replaced with EffNetV2 and SwinT, the diagnostic performance improved significantly, with SwinT outperforming EffNetV2 slightly. The SwinT model effectively focused on global features through its shifting window mechanism, capturing the correlation between multi-point fault features. In contrast, the proposed DVIT method fully explored the correlation of multi-point information in the time-frequency images, ultimately achieving an average accuracy of 94.01%.

In the dual dataset experiment, the overall trend was similar to that of the single dataset experiment. With the increase in the number and types of datasets, more local similar features were provided, resulting in a 5% increase in the accuracy of both the traditional CNN and EffNetV2. SwinT was the most sensitive to the number of datasets, achieving an accuracy of 94.12%. In contrast, the DVIT method proposed in this study performed exceptionally well in the dual dataset experiment, ultimately achieving an average accuracy of 97.85%.

In summary, the results of the variable load experiment show that the method proposed in this study exhibits the highest average accuracy under changing circuit operating conditions. It is better able to adapt to fault states that occur in actual circuit operations, demonstrating exceptional generalization ability and robustness.

V. CONCLUSION

This study has introduced the IWT-DVIT diagnostic system specifically designed for multi-stage conversion circuits. The system has employed an innovative IWT data fusion scheme to synchronize, decompose, and recombine multiple time series signals for surface-level data integration. Additionally, the study has incorporated the DVIT algorithm, which is equipped with dual-axis observation encoders and axial data decoders. This has allowed for the analysis of deep features through the interaction of time-domain and frequency-domain information, thereby effectively diagnosing faults. Experimental results within the LLC Series Resonant Converter have demonstrated that, compared to traditional diagnostic methods, this diagnostic system has significantly enhanced the reliability and accuracy of fault detection. Future work will explore the performance of this method on other converter components, as well as its potential in unsupervised diagnostic research [4], [35], [37], [19] fault-tolerant control [42], [6], [22] and real-time fault detection [1], [36].

REFERENCES

[1] S. Ahmadi, P. Poure, S. Saadate and D. A. Khaburi, A real-time fault diagnosis for neutral-point-clamped inverters based on failure-mode algorithm, *IEEE Transactions on Industrial Informatics*, vol. 17, no. 2, pp. 1100–1110, Feb. 2021.

[2] M. Ai, Y. Xie, Z. Tang, J. Zhang and W. Gui, Two-stream deep feature-based froth flotation monitoring using visual attention clues, *IEEE Transactions on Instrumentation and Measurement*, vol. 70, art. no. 9502114, Sept. 2021.

[3] S. Biswas, G. K. Mahanti and N. Chattaraj, Investigation of extreme learning machine-based fault diagnosis to identify faulty components in analog circuits, *Circuits, Systems, and Signal Processing*, vol. 43, pp. 711–728, Oct. 2024.

[4] H. Chen, Z. Liu, C. Alippi, B. Huang and D. Liu, Explainable intelligent fault diagnosis for nonlinear dynamic systems: From unsupervised to supervised learning, *IEEE Transactions on Neural Networks and Learning Systems*, vol. 35, no. 5, pp. 6166–6179, May. 2024.

[5] C. Chen, F. Shen, J. Xu and R. Yan, Probabilistic latent semantic analysis-based gear fault diagnosis under variable working conditions, *IEEE Transactions on Instrumentation and Measurement*, vol. 69, no. 6, pp. 2845–2857, June. 2020.

[6] G. F. Cui, L. B. Wu and M. Wu, Adaptive event-triggered fault-tolerant control for leader-following consensus of multi-agent systems, *International Journal of Systems Science*, vol. 55, no. 15, pp. 3291–3303, 2024.

[7] R. Das and H. Le, Gate driver circuits with discrete components for GaN-based multilevel multi-inductor hybrid converter, *IEEE Transactions on Industrial Electronics*, vol. 70, no. 2, pp. 1105–1114, Feb. 2023.

[8] M. Gong, L. Sheng and D. Zhou, Robust fault-tolerant stabilisation of uncertain high-order fully actuated systems with actuator faults, *International Journal of Systems Science*, vol. 55, no. 12, pp. 2518–2530, 2024.

[9] W. Han, L. Cheng, W. Han, C. Yu, Z. Hao and Z. Yin, Soft fault diagnosis for DC–DC converter based on improved ResNet-50, *IEEE Access*, vol. 11, pp. 81157–81168, Aug. 2023.

[10] W. Han, W. Han, L. Cheng, W. Han, C. Yu, Z. Yin, Z. Hao and J. Zhu, Incipient fault diagnosis for DC–DC converter based on multi-dimensional feature fusion, *IEEE Access*, vol. 11, pp. 58822–58834, June. 2023.

[11] W. He, Y. He and B. Li, Generative adversarial networks with comprehensive wavelet feature for fault diagnosis of analog circuits, *IEEE Transactions on Instrumentation and Measurement*, vol. 69, no. 9, pp. 6640–6650, Sept. 2020.

[12] Y. Hou, Z. Wu, X. Cai and Z. Dong, Prediction method of soft fault and service life of DC-DC converter circuit based on improved support vector machine, *Entropy*, vol. 24, no. 3, art. no. 402, Mar. 2022.

[13] Y. Jiang, L. Xia and J. Zhang, A fault feature extraction method for DC–DC converters based on automatic hyperparameter-optimized 1-D convolution and long short-term memory neural networks, *IEEE Journal of Emerging and Selected Topics in Power Electronics*, vol. 10, no. 4, pp. 4703–4714, Aug. 2022.

[14] J. Jiang, J. Zhu, M. Bilal, Y. Cui, N. Kumar, R. Dou, F. Su and X. Xu, Masked swin transformer unet for industrial anomaly detection, *IEEE Transactions on Industrial Informatics*, vol. 19, no. 2, pp. 2200-2209, Feb. 2023.

[15] J. H. Lee and B. H. Cho, Large time-scale electro-thermal simulation for loss and thermal management of power MOSFET, *Proceedings of IEEE 34th Annual Conference on Power Electronics Specialist*, pp. 112–117, 2003.

[16] Z. Li, Y. Gao, X. Zhang, B. Wang and H. Ma, A model-data-hybrid-driven diagnosis method for open-switch faults in power converters, *IEEE Transactions on Power Electronics*, vol. 36, no. 5, pp. 4965–4970, May. 2021.

[17] Z. Liu, X. Liu, S. Xie, J. Wang and X. Zhou, A novel fault diagnosis method for analog circuits based on multi-input deep residual networks with an improved empirical wavelet transform, *Applied Sciences*, vol. 12, no. 3, art. no. 1675, Feb. 2022.

[18] Y. Lian, L. Xie, S. Han, F. Du, Y. Wang and Z. Lu, Advances in postprocessing technology for laser ultrasound detection signals: a review, *IEEE Sensors Journal*, vol. 23, no. 23, pp. 28564–28578, Dec. 2023.

[19] J. Liao, H. K. Lam, S. Gulati and B. Hayee, Improved computer-aided diagnosis system for nonerosive reflux disease using contrastive self-supervised learning with transfer learning, *International Journal of Network Dynamics and Intelligence*, vol. 2, no. 3, art. no. 100010, Sep. 2023.

[20] C. Li, Y. Liu, M. Gao and L. Sheng, Fault-tolerant formation consensus control for time-varying multi-agent systems with stochastic communication protocol, *International Journal of Network Dynamics and Intelligence*, vol. 3, no. 1, art. no. 100004, Mar. 2024.

[21] Y. Li, R. Zhang, Y. Guo, P. Huan and M. Zhang, Nonlinear soft fault diagnosis of analog circuits based on RCCA-SVM, *IEEE Access*, vol. 8, pp. 60951–60963, Mar. 2020.

[22] M. Li, K. Zhang, Y. Ma and B. Jiang, Prescribed-time fault-tolerant control for the formation of quadrotors based on fully-actuated system

approaches, *International Journal of Systems Science*, vol. 55, no. 12, pp. 2541–2555, 2024.

[23] S. Ma and Y. Li, Adaptive fuzzy fault-tolerant control for active seat suspension systems with full-state constraints, *Systems Science & Control Engineering*, vol. 11, no. 1, art. no. 2153391, 2023.

[24] C. Mishra, A. K. Samantaray and G. Chakraborty, Rolling element bearing fault diagnosis under slow speed operation using wavelet denoising, *Measurement*, vol. 103, pp. 77–86, Aug. 2017.

[25] M. Parai, S. Srimani, K. Ghosh and H. Rahaman, Multi-source data fusion technique for parametric fault diagnosis in analog circuits, *Integration*, vol. 84, pp. 92–101, May. 2022.

[26] M. Ragab, Z. Chen, W. Zhang, E. Eldele, M. Wu, C. Kwoh and X. Li, Conditional contrastive domain generalization for fault diagnosis, *IEEE Transactions on Instrumentation and Measurement*, vol. 71 art. no. 3506912, Feb. 2022.

[27] M. M. Rahman and M. N. Uddin, Online unbalanced rotor fault detection of an IM drive based on both time and frequency domain analyses, *IEEE Transactions on Industry Applications*, vol. 53, no. 4, pp. 4087–4096, Aug. 2017.

[28] L. Shao, J. He, X. Lu, B. Hei, J. Qu and W. Liu, Aircraft skin damage detection and assessment from UAV images using GLCM and cloud model, *IEEE Transactions on Intelligent Transportation Systems*, vol. 25, no. 3, pp. 3191–3200, Mar. 2024.

[29] A. Shaker, S. T. Wasim, S. Khan, J. Gall and F. S. Khan, GroupMamba: Efficient group-based visual state space model, *arXiv preprint arXiv: 2407.13772*, 2025.

[30] Y. Tan, E. Hu, Y. Liu, J. Li and W. Chen, Review of digital vibration signal analysis techniques for fault diagnosis of high-voltage circuit breakers, *IEEE Transactions on Dielectrics and Electrical Insulation*, vol. 31, no. 1, pp. 404–418, Feb. 2024.

[31] S. Tian, F. C. Lee and Q. Li, Equivalent circuit modeling of LLC resonant converter, *IEEE Transactions on Power Electronics*, vol. 35, no. 8, pp. 8833–8845, Aug. 2020.

[32] Y. Wang, Y. Guan, M. Molinas, O. B. Fosso, W. Hu and Y. Zhang, Open-circuit switching fault analysis and tolerant strategy for dual-active-bridge DC–DC converter considering parasitic parameters, *IEEE Trans. Power Electron.*, vol. 37, no. 12, pp. 15020–15034, Dec. 2022.

[33] S. Wang, Z. Liu, Z. Jia and Z. Li, Incipient fault diagnosis of analog circuit with ensemble HKELM based on fused multi-channel and multi-scale features, *Engineering Applications of Artificial Intelligence*, vol. 117, art. no. 105633, Jan. 2023.

[34] H. Wang, Z. Liu, D. Peng and Y. Qin, Understanding and learning discriminant features based on multiattention 1D-CNN for wheelset bearing fault diagnosis, *IEEE Transactions on Industrial Informatics*, vol. 16, no. 9, pp. 5735–5745, Sept. 2020.

[35] C. Wang, Z. Wang, H. Liu, H. Dong and G. Lu, An optimal unsupervised domain adaptation approach with applications to pipeline fault diagnosis: balancing invariance and variance, *IEEE Transactions on Industrial Informatics*, vol. 20, no. 8, pp. 10019–10030, Aug. 2024.

[36] L. Wang, W. Sun and H. Pei, Nonlinear disturbance observer-based geometric attitude fault-tolerant control of quadrotors, *International Journal of Systems Science*, vol. 55, no. 11, pp. 2337–2348, 2024.

[37] C. Wang, Z. Wang, Q. Liu, H. Dong and W. Sheng, Support-sample-assisted domain generalization via attacks and defenses: concepts, algorithms and applications to pipeline fault diagnosis, *IEEE Transactions on Industrial Informatics*, vol. 20, no. 4, pp. 6413–6423, Apr. 2024.

[38] Y. Wang, C. Wen and X. Wu, Fault detection and isolation of floating wind turbine pitch system based on Kalman filter and multi-attention 1DCNN, *Systems Science & Control Engineering*, vol. 12, no. 1, art. no. 2362169, 2024.

[39] N. Yang, J. Liu, W. Zhao and Y. Tan, Fault diagnosis of gear based on multichannel feature fusion and DropKey-vision transformer, *IEEE Sensors Journal*, vol. 24, no. 4, pp. 4758–4770, Feb. 2024.

[40] C. Yang, S. Tian, B. Long and F. Chen, Methods of handling the tolerance and test-point selection problem for analog-circuit fault diagnosis, *IEEE Transactions on Instrumentation and Measurement*, vol. 60, no. 1, pp. 176–185, Jan. 2011.

[41] C. Yang, Z. Wu, T. Peng, H. Zhu and C. Yang, A fractional steepest ascent Morlet wavelet transform-based transient fault diagnosis method for traction drive control system, *IEEE transactions on transportation electrification*, vol. 7, no. 1, pp. 147–160, Mar. 2021.

[42] Z. Ye, Z. Yu, Y. Cheng and B. Jiang, Finite-time sliding-mode observer based distributed robust fault tolerant control for multi-agent systems against actuator and sensor faults, *International Journal of Systems Science*, vol. 55, no. 4, pp. 618–630, 2024.

[43] R. Yu, W. Yu and X. Wang, KAN or MLP: A fairer comparison, *arXiv preprint arXiv: 2407.16674*, 2024.

[44] T. Zhang, L. Li, Y. Zhou, W. Liu, C. Qian, J. Hwang and X. Ji, CAS-ViT: Convolutional additive self-attention vision transformers for efficient mobile applications, *arXiv preprint arXiv: 2408.03703*, 2024.

[45] L. Zhou and M. Preindl, A multilayer software-defined system for high-performance electric vehicle energy conversion, *IEEE Transactions on Transportation Electrification*, vol. 9, no. 3, pp. 3867–3879, Sept. 2023.

Li Wang (Member, IEEE) received the Ph.D. degree in control science and engineering from the College of Electronics and Information Engineering, Tongji University, Shanghai, China, in 2019. He has published over 20 scientific papers in journals and international conferences. He is currently a Lecturer and a Graduate Advisor with the School of Electrical Engineering and Automation, Nantong University, Nantong, China. His research interests focus on the prognostics and health management of power electronic circuits, advanced measurement and control technologies, failure diagnosis algorithms, and design for embedded systems.
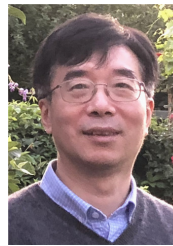
Zidong Wang (Fellow, IEEE) is currently a Professor of dynamical systems and computing with the Department of Computer Science, Brunel University London, Uxbridge, U.K. He has authored a number of articles in international journals. He is a member of the Academia Europaea and the European Academy of Sciences and Arts, an Academician of the International Academy for Systems and Cybernetic Sciences, a fellow of the Royal Statistical Society, and a member of the program committee for many international conferences. He serves (or has served) as the Editor-in-Chief for International Journal of Systems Science, Neurocomputing, and Systems Science and Control Engineering.

Chao Xu received the B.S. degree in Electrical Engineering and Automation from Nantong University, Jiangsu, China, in 2017. Since June 2022, he has been pursuing a Master's degree in Control Science and Engineering at Nantong University in Jiangsu, China. His research interests include failure detection of power electronic converters, on-line health monitoring technology, deep learning and embedded system design.

Guoping Lu received the B.S. degree from the Department of Applied Mathematics, Chengdu University of Science and Technology, China, in 1984, and the M.S. and Ph.D. degrees from the Department of Mathematics, East China Normal University, China, in 1989 and 1998, respectively. He is currently a Professor with the School of Electrical Engineering and Automation, Nantong University, Jiangsu, China. His current research interests include singular systems, multiagent systems, networked control, and nonlinear signal processing.

Liang Hua received the B.S. degree in the School of Electrical Engineering and Automation from Nantong University, Nantong, China, in 2001, and the M.S. and Ph.D. degrees in control engineering from the Zhejiang University of Technology, Hangzhou, China, in 2008 and 2014, respectively. In 2001, he joined a Faculty Member of Nantong University, where he is currently a Professor of Electrical Engineering. He is a member of the Youth Working Committee of the Chinese Society of Automation, and a high-level talent in the "Six Talents" peak of Jiangsu Province, Executive Director of Jiangsu Electrotechnical Society. His research interests include power system optimization, renewable power generation, and energy storage systems.